J Mater Sci

Energy materials

Heterostructured $CoSe_2$/Se/hollow carbon spheres as a superior sulfur host for lithium–sulfur batteries

Jihan Li[1], Han Su[1], Mingzhi Yang[1], Weiliang Liu[1], Feipeng Cai[1], Jinshui Yao[1], Manman Ren[1,*], and Yuanhao Wang[2,*]

[1] *School of Materials Science and Engineering, Energy Institute, Qilu University of Technology (ShandongAcademy of Sciences), Jinan 250353, People's Republic of China*

[2] *Hoffmann Institute of Advanced Materials, Shenzhen Polytechnic, 7098 Liuxian Boulevard, Nanshan District, Shenzhen 518055, People's Republic of China*

Received: 19 February 2023
Accepted: 24 May 2023

ABSTRACT

Owing to the high energy density, lithium–sulfur batteries (LSBs) have attracted a lot of attention as a representative of new secondary batteries. However, LSBs also face some serious issues in practical applications such as the large volume expansion of S cathode, shuttle effect of lithium polysulfide (LPSs), and dendrite formation of lithium metal anode. In this work, hollow carbon sphere (HCS) was used as a framework, and $CoSe_2$/Se nanorods were uniformly loaded on the HCS surface to form a 3D heterostructured composite (CS/Se/HCS). When used as an active sulfur host, the HCS is conducive to the transport of electrons and Li^+; meanwhile, it can suppress the large volume expansion in the electrochemical performance. $CoSe_2$ can effectively adsorb LPSs and accelerate the transformation of LPSs. We also investigated the effect of $CoSe_2$/Se content on the electrochemical performance of the S electrode. Among different CS/Se/HCS samples, the CS/Se/HCS-0.3/S electrode exhibited the best electrochemical performance; at 1C rate, after 500 cycles, it presents a reversible capacity of 511 mA h g^{-1}. This work provided a new idea for the combination of transition metal selenide and carbon materials, which can be used in LSBs and other energy storage devices.

Handling Editor: Naiqin Zhao.

Jihan Li and Han Su have contributed equally to this work.

Address correspondence to E-mail: renmanman@qlu.edu.cn; wangyuanhao@szpt.edu.cn

https://doi.org/10.1007/s10853-023-08631-z

Published online: 05 June 2023

GRAPHICAL ABSTRACT

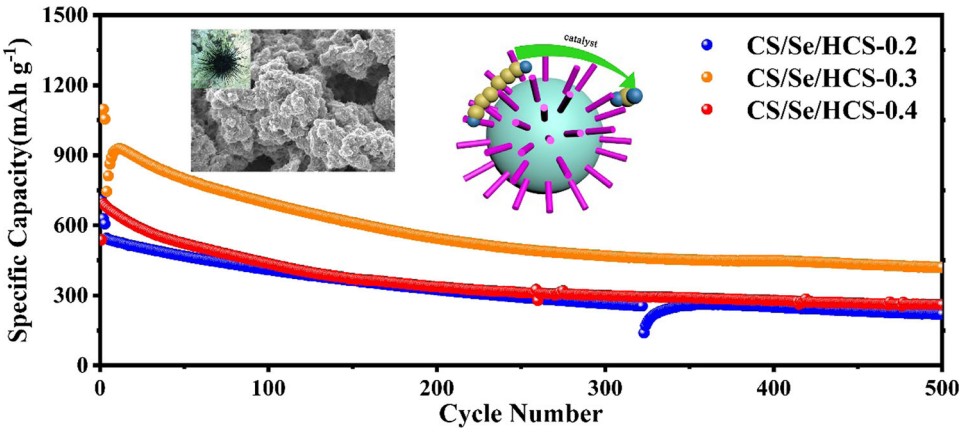

Introduction

Due to the excessive burning of fossil fuels and the rapidly growing demand for renewable energy, traditional Li-ion batteries can no longer meet the needs of some energy storage equipment, and numerous new batteries have appeared one after another [1–3]. Among the novel batteries, Li–S batteries (LSBs) with high energy density (2600 Wh g^{-1}), wide availability, and low price are considered one of the most promising new secondary batteries [4, 5]. However, in the practical application of LSBs, S cathode encountered some serious issues such as volume expansion, the "shuttle effect" of lithium polysulfides (LPSs), and poor conductivity [6–8]. Large volume expansion will destroy the structure of the electrode, leading to poor cycling stability; the "shuttle effect" of LPSs results in the reduction of coulombic efficiency and capacity; and the low electronic conductivity will seriously affect the rate performance of S cathodes [9–12].

In the past few years, to overcome these issues, carbon-based materials such as carbon spheres, carbon tubes, graphene oxide, and carbon nanocages were investigated as S hosts, these carbon-based materials can significantly relieve the volume expansion and improve the conductivity of S cathodes [13–17]. However, because of the weak adsorption ability of nonpolar carbon materials for polar LPSs, the shuttle of LPSs was not well suppressed [18, 19]. Later, researchers found that N, P, or other elements doping can enhance the polarity of carbon-based materials; meanwhile, the heterogeneous element-doped carbon materials have a certain adsorption capacity for LPSs [20]. Although heteroelement doping has a certain effect, the adsorption of LPSs is still not obvious [21].

To enhance the adsorption of carbon-based materials toward LPSs, many polar compounds including oxides [22, 23], sulfides [24, 25], hydroxides [26, 27], nitrides [28], etc. were introduced to the carbon-based hosts. Experiments and theoretical calculations testified that these compounds showed strong chemical adsorption for LPSs. At the same time, these compounds can accelerate the conversion of LPSs to Li_2S, thereby effectively inhibiting the "shuttle effect" [29, 30]. Among the polar compounds, because of the similar atomic structure and electron distribution between selenium and sulfur, selenides exhibit better adsorption and electrochemical catalysis for LPSs. Additionally, selenides show great application potential in LSBs due to the better electronic conductivity, [12, 31–33]. Li et al. [34] designed a B, N-codoped carbon nanotube array decorated with sulfilic and lithiophilic CoSe nanoparticles grown on carbon cloth (CoSe@BNCNTs/CC) as both sulfur and lithium hosts. The assembled Li–S full battery with the CoSe@BNCNTs/CC dual-functional host exhibited long-term cycling stability (800 cycles at 0.5 C

with a decay rate of 0.066% per cycle). Once we designed and prepared a $CoSe_2$/N-doped hollow carbon tube ($CoSe_2$/hNCTs) S host. At 3C, the $CoSe_2$/hNCTs-S electrode delivers excellent high rate performance. And theoretical calculations also testified the excellent adsorption and electrocatalytic performance of $CoSe_2$ on LPSs [6].

It is reported that hollow structured materials are favorable for sulfur loading and effective physical confinement toward LPSs [35, 36]. Moreover, heterostructured S hosts demonstrated excellent electrochemical performance, because the heterostructure can deform the interface and change the charge distribution, thereby accelerating the diffusion of Li^+ and reducing the energy barrier of electrochemical reactions. For example, Ye and his team prepared heterostructured CoSe/ZnSe anchored on graphene aerogels and used it as a S host; at 2 C, the CoSe/ZnSe-S electrode exhibited a very low average capacity decay rate of 0.027% over 1700 cycles [37].

In this work, we carried out the related exploration of heterostructured $CoSe_2$ and successfully prepared a $CoSe_2$/Se/carbon hollow spheres (CS/Se/HCS) heterostructure composite by using SiO_2 spheres as templates, and the composite was applied as a S host for LSBs. The hollow carbon spheres can provide high electronic conductivity and alleviate the large volume change during the intercalation/deintercalation of lithium. The $CoSe_2$/Se attached on the HCS surface can effectively adsorb LPSs and accelerate theris conversion. Additionally, we also investigated the effect of $CoSe_2$/Se content on the lithium storage performance. Among different CS/Se/HCS samples, the CS/Se/HCS-0.3/S electrode exhibited the best electrochemical performance. At 1 C rate, after 500 cycles, it can present a reversible capacity of 511 mA h g^{-1}. The CS/Se/HCS-0.3/S electrode also exhibits a reversible capacity of 480 mA h g^{-1} after 200 cycles at a high rate of 3 C.

Experimental section

Synthesis CS/Se/HCS host

Firstly, 12 mmol tetrapropoxysilane was dispersed and stirred in a mixed solution of 10 mL deionized water, 70 mL ethanol, and 3 mL ammonia water (wt = 25%) at 25 °C; then, 0.56 mL formaldehyde (wt = 37%), 0.4 g resorcinol, and 0.3 g cobalt nitrate hexahydrate were added to the mixed solution and stirred for 24 h, then washed with ethanol and deionized water, and dried at 50 °C overnight to obtain a black SiO_2@Phenolic Resin/Cobalt compound (SiO_2@PR/CC) precursor. The precursor was calcined in Ar at 700 °C for 5 h to obtain the SiO_2@C/Co intermediate. Next the SiO_2@C/Co intermediate was etched with 2 mol L^{-1} sodium hydroxide solution to remove the SiO_2 core. After removing the SiO_2 core, we got the Co/ hollow carbon spheres (Co/HCS).

Different CS/Se/HCS samples were obtained by heating Co/HCS and selenium powder with a mass ratio of 1:2 in Ar at 350 °C for 3 h. The amounts of cobalt source were 0.2, 0.3, and 0.4 g, and the corresponding products were named CS/SeHCS-0.2, CS/Se/HCS-0.3, and CS/Se/HCS-0.4, respectively.

Preparation of CS/Se/HCS/S electrodes

30 wt% CS/Se/HCS was mixed with 70 wt% S powder and heated at 155 °C for 12 h under Ar. After cooling, the mixture was reheated at 200 °C for 30 min to remove the excess S. The electrodes were composed of CS/Se/HCS/S (70 wt%), acetylene black (20 wt%), and polyvinylidene fluoride (10 wt%). The preparation procedure was the same as our previous report [38]. The diameter of each electrode was 12 mm and the thickness was 200–400 nm, where the active substance sulfur loading was 1.0–3.0 mg cm^{-2}.

Material characterization

Shimadzu XRD-6100AS XRD Diffractometer with Cu Ka radiation (λ = 1.54 Å) was used to investigate the phase structure of the prepared samples. The scanning speed was 6° min^{-1} with a scanning range of 10–80°. The Raman spectrum was obtained by LabRam HR Evolution and the test laser wavelength was 532.03 nm. Thermogravimetric (TG) analysis was characterized by a METTLER TOLEDO thermogravimetric analyzer under Ar atmosphere. The heating rate was 10° min^{-1} and the temperature range was 25–600 °C. An ultraviolet spectrophotometer (TU-1901) was employed for the ultraviolet test in the LPSs adsorption experiment. N_2 adsorption and desorption isotherms were tested by Micromeritcs GeminiV2380 analyzer operated at

77 K. ESCALAB 250 spectrometer was employed to measure X-ray photoelectron spectroscopy (XPS). Monochromatic Al Kα (1486.6 eV) was used as the X-ray emission source with a step size of 0.05 eV. Scanning electron microscope (ZEISS G500) and transmission electron microscope (FEI-TECNAI-G20) were utilized to observe the morphologies of the samples. The element distribution was also measured on FEI-TECNAI-G20. The accelerating voltage of the SEM is 5–15 kV, the working distance was 10 mm and the high resolution was 4 mm. The accelerating voltage of the TEM test was 200 kV.

Electrochemical test

The electrochemical performances of the CS/Se/HCS/S electrodes were evaluated by typical CR2032 simulated batteries. The charging/discharging performance of simulated batteries was recorded by the NEWARE battery test system in a potential range of 1.7–2.8 V (vs. Li^+/Li) at different C rates under 25 °C. Electrochemical impedance spectroscopy (EIS) and cyclic voltammetry (CVs) were carried out on the CHI760E electrochemical workstation. 1.0 M LiTFSI in DME: DOL = 1:1 Vol% with 5.0% $LiNO_3$. Celgard 2400 and metal Li were used as separator and counter electrode, respectively. The electrolyte dosage was accurately controlled with an electrolyte/sulfur ratio ≈55 μL mg^{-1} under normal conditions.

Results and discussions

The preparation process of the CS/Se/HCS host is presented in scheme 1. Firstly, SiO_2 spheres are synthesized, and then, phenol and formaldehyde are in situ polymerized on the SiO_2 surface to form SiO_2@PR; meanwhile, cobalt salt is supported on the SiO_2@PR to form SiO_2@PR/CC precursor. Next, the SiO_2@PR/CC precursor is transformed into SiO_2@C/Co intermediate under the calcination process. After etching the SiO_2@C/Co intermediate with 2 mol L^{-1} sodium hydroxide solution, the Co/HCS is obtained. The final CS/Se/HCS is obtained by further selenization.

The chemical composition and crystal structure of the samples were studied by XRD analysis. All the main peaks of the three samples in Fig. 1a can correspond to $CoSe_2$ (JCPDS card No. 53-0449) or Se (JCPDS card No. 06-0362). Owing to the carbon in the CS/Se/HCS is amorphous, there is no obvious carbon peaks. The diffraction peaks attributed to $CoSe_2$ and Se in CS/Se/HCS-0.3 are significantly stronger than those of the other two samples, indicating that its crystallinity and phase purity is higher. Figure 1b exhibits the Raman spectra of CS/Se/HCS-0.2/0.3/0.4 samples, in which the two broad peaks at 1337 and 1585 cm^{-1} correspond to the defect state (D band) and graphitization state (G band) of carbon [39], and the other peak at 669 cm^{-1} is assigned to $CoSe_2$ [40]. I_D/I_G implies the defect degree in carbon materials; it is obvious that CS/Se/HCS-0.3 exhibits more defects, which is beneficial to increase the electronic conductivity of the materials [41].

The TG test under N_2 was employed to determine the active S content in CS/Se/HCS-0.3/S electrode. According to the TG results, the S content in the CS/Se/HCS-0.3/S host is 63%, indicating the excellent sulfur storage capacity of the CS/Se/HCS-0.3 host (Figure S1). Figure 1c indicates the nitrogen adsorption/desorption isotherms of CS/Se/HCS-0.2/0.3/0.4. The isotherms of the three samples are all of V type with H3-type hysteresis loops. Among them, CS/Se/HCS-0.3 exhibits a higher specific surface area (9.7 m^2 g^{-1}) than the other two samples (4.3 and 6.7 m^2 g^{-1}), which is beneficial to improve the active sites. The average pore size and pore volume of the CS/Se/HCS-0.3 are about 26.5 nm and 0.04 cm^3 g^{-1}, respectively, indicating that the CS/Se/HCS-0.3 has mesoporous structure. And the suitable pore structure is beneficial for sulfur storage and electrolyte wetting.

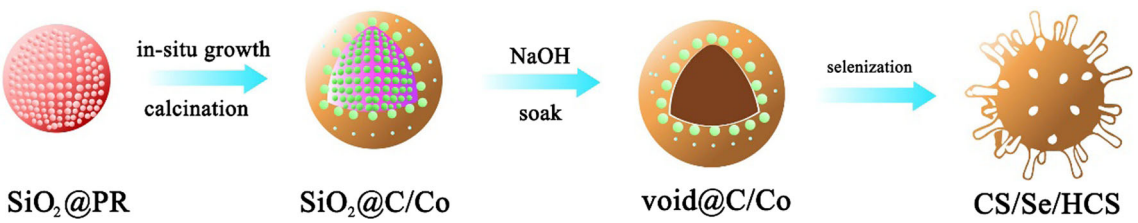

Scheme 1 Synthesis process of the CS/Se/HCS.

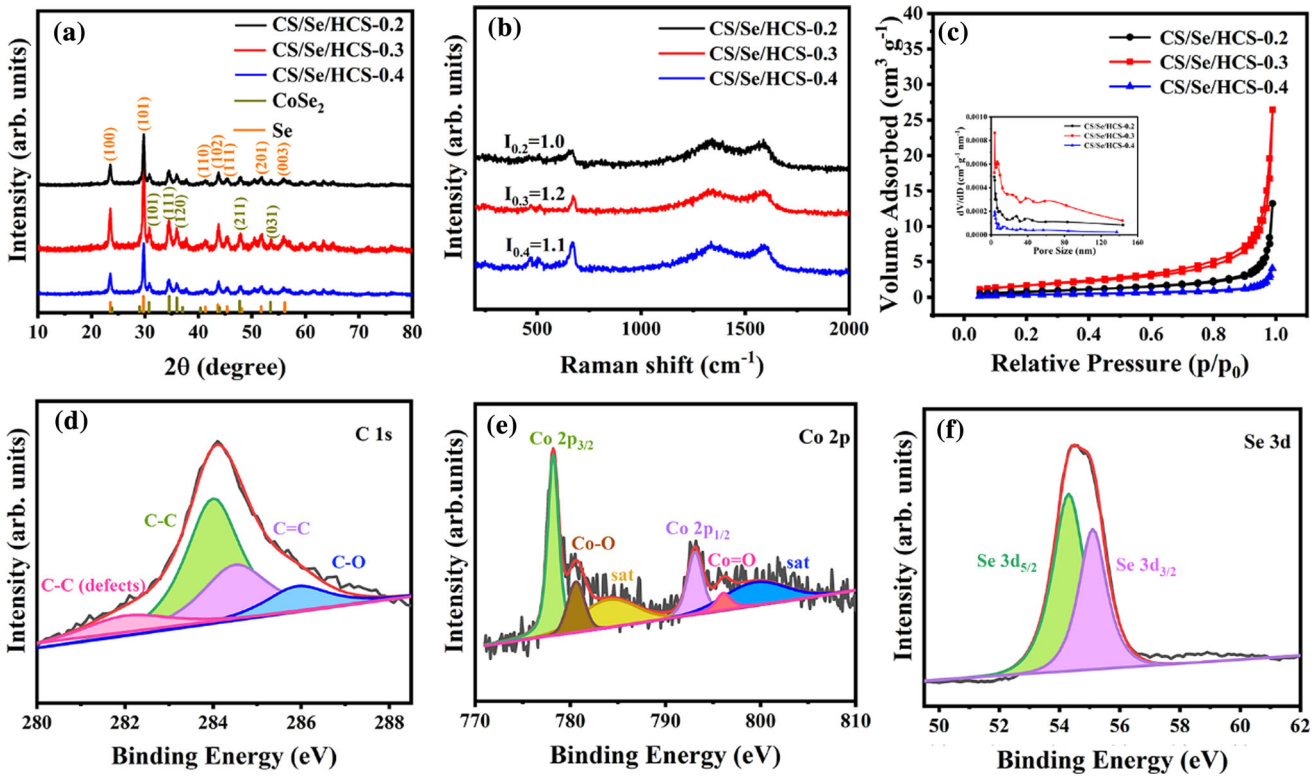

Figure 1 XRD patterns (**a**), Raman spectra (**b**), and N_2 adsorption/desorption isotherms and pore size distribution (inset) (**c**) of the CS/Se/HCS-0.2/0.3/0.4. XPS spectra of C1s (**d**), Co2p (**e**), and Se3d (**f**) in the CS/Se/HCS-0.3.

Figure 1d demonstrates the high-resolution C1s XPS spectrum in CS/Se/HCS-0.3, in which the main three broad peaks appear at 282.0, 283.9, 284.5, and 285.9 eV are ascribed to C–C (defects), C–C, C=C, and C-O, respectively [42, 43]. Among them, C–C mainly comes from the hollow carbon spheres, C=C is attributed to the oxidation of part of C–C during the calcination process, and the C–O is generated due to the partial oxidation in the surface of CS/Se/HCS during the experiment process. The high-resolution Co2p XPS spectrum manifests that the binding energies of $Co2p_{3/2}$ and $Co2p_{1/2}$ appear at 778.2 and 793.1 eV, and their satellite peaks appear at 784.0 and 801.1 eV, consistent with the peak positions in the literature [44]. The result confirms the presence of Co^{2+} cations in CS/Se/HCS-0.3 (Fig. 1e). Additionally, two other peaks at 780.6 and 796.1 eV are assigned to Co–O (III) and Co = O bonds, respectively [39, 45, 46]. Two main broad peaks at 54.3 and 55.0 eV in the high-resolution Se3d XPS spectrum belong to $Se3d_{5/2}$ and $Se3d_{3/2}$, respectively, which are matched with the metal–Se bond (Fig. 1f) [47, 48]. The spin–orbit splitting of 0.7 eV between $Se3d_{5/2}$ and $Se3d_{3/2}$ peaks is attributed to metallic selenium [49]. The XPS result also certifies the coexistence of $CoSe_2$ and Se.

The morphologies of HCS and CS/Se/HCS-0.2/0.3/0.4 are observed by SEM tests. HCS shows monodisperse spherical morphology (Figure S2). Figure 2a–c exhibits the surface morphologies of CS/Se/HCS-0.2/0.3/0.4 samples. It can be clearly observed that all the samples exhibit a 3D spherical structure. For CS/Se/HCS-0.2, only a small number of carbon spheres are detected loaded with other substances (Fig. 2a), which is due to the small amount of cobalt source. Compared with CS/Se/HCS-0.2, more nanorods are uniformly loaded on the hollow carbon sphere surface (Fig. 2b), additionally, and the hollow carbon spheres are connected together. However, for CS/Se/HCS-0.4, due to excess cobalt source the spherical structure is destroyed, and severe aggregation is detected (Fig. 2c). The 3D structure is beneficial to the transport of electrons and Li^+; meanwhile, it also can inhibit the large volume variation of the S cathode during the electrochemical process. The exposed $CoSe_2$/Se nanorods on the HCS surface can capture LPSs and accelerate their conversion simultaneously. Furthermore, the

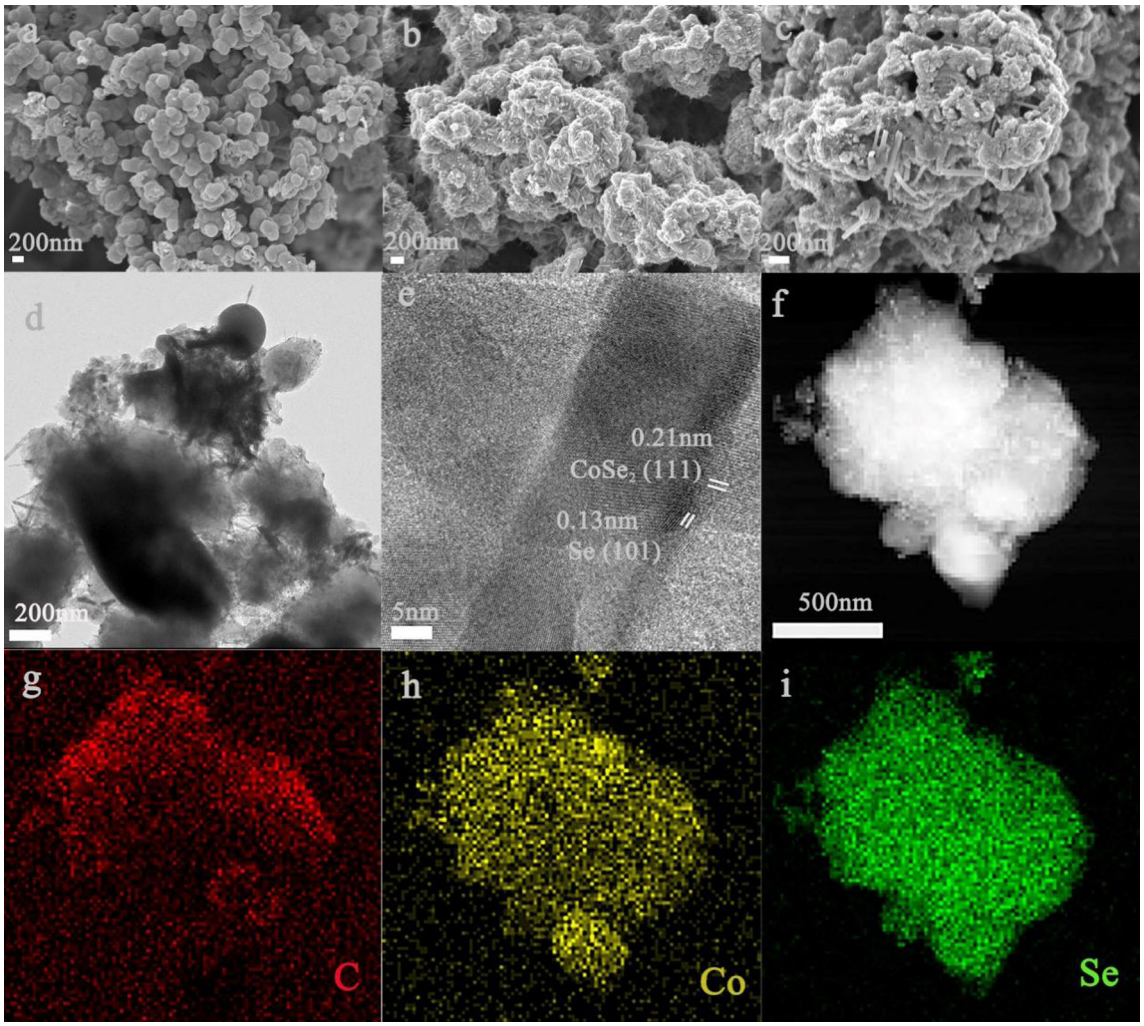

Figure 2 SEM images of the CS/Se/HCS-0.2 (**a**), CS/Se/HCS-0.3 (**b**), and CS/Se/HCS-0.4 (**c**). TEM (**d**), HRTEM (**e**), HAADF-STEM (**f**), and EDS mapping (**g**–**i**) of the CS/Se/HCS-0.3.

morphology of the CS/Se/HCS-0.3/S electrode was also characterized by SEM. As shown in Figure S3, the morphology of the CS/Se/HCS-0.3/S is basically the same as that of the CS/Se/HCS-0.3 host, illustrating that there are a small amount of sulfur on the surface of CS/Se/HCS-0.3 and a large amount inside the hollow/microporous structure of HCS. This also testifies the excellent sulfur storage performance of the CS/Se/HCS-0.3 host.

The microstructure of CS/Se/HCS-0.3 was further observed by the TEM test. Under low-magnification TEM image, the CS/Se/HCS-0.3 exhibits an irregular 3D spherical structure, and some nanorods are scattered on the HCS surface. Maybe due to the sonication during the TEM test resulted in the destruction of the sample structure, the hollow structure of carbon is not obvious (Fig. 2d). The obvious interplanar distances of 0.21 and 0.13 nm in HRTEM are well matched to the (111) plane of $CoSe_2$ and the (101) plane of Se, respectively (Fig. 2e). Figure 2g–i illustrates the EDS elemental mappings of the C, Se, and Co, respectively. In C element mapping, the color of the edge is heavier than the center, further demonstrating the hollow structure of the carbon spheres. However, the Se and Co are uniformly distributed throughout the structure, indicating that Se and $CoSe_2$ exist not only on the surface of HCS but also in the interior of HCS. The HCS can provide a highly conductive network and prevent the LPSs from shuttling by physical confinement. $CoSe_2$/Se distributed on the HCS can effectively adsorb LPSs through chemical adsorption and accelerate its conversion. Thereby, CS/Se/HCS can effectively relieve the "shuttle effect."

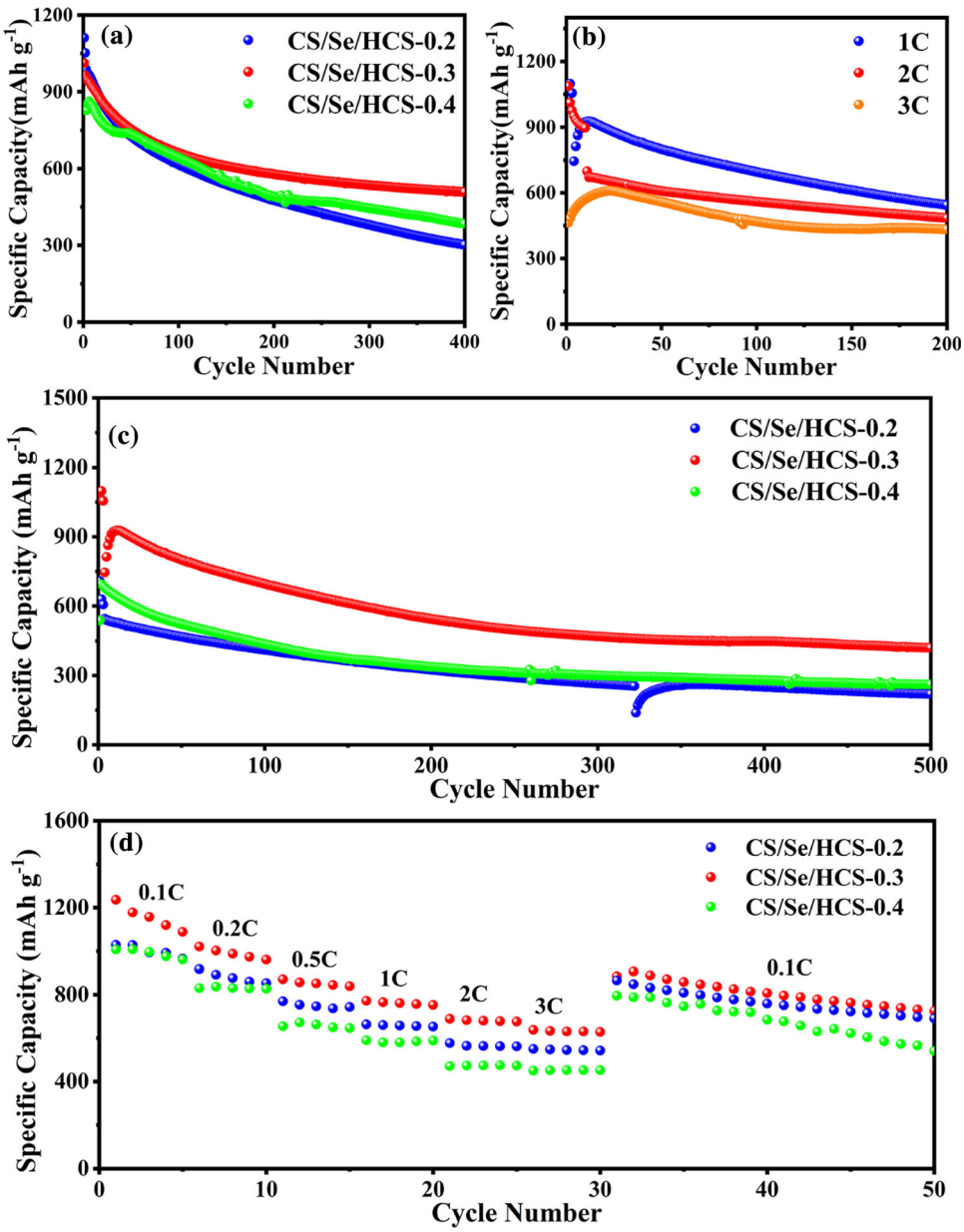

Figure 3 **a** Cycling performance of the CS/Se/HCS-0.2/0.3/0.4/S electrodes at 0.5C. **b** Cycling performance of the CS/Se/HCS-0.3/S electrode at different C rates. **c** Cycling stability of the CS/Se/HCS-0.2/0.3/0.4/S electrodes at 1C. **d** Rate performance of the CS/Se/HCS-0.2/0.3/0.4/S electrodes at different C rates.

Figure 3a illustrates the cycling performances of the CS/Se/HCS-0.2/0.3/0.4/S electrodes at 0.5 C. The CS/Se/HCS-0.3/S electrode presents a high initial discharge specific capacity of 1012 mA h g^{-1} and a high initial coulombic efficiency of 94%. After 400 cycles, the specific capacity can be maintained at 511 mA h g^{-1}. However, the specific capacities of the CS/Se/HCS-0.2/S and CS/Se/HCS-0.4/S electrodes are 293 and 378 mA h g^{-1} after 400 cycles, respectively. The electrochemical performance at high rates is an important indicator for evaluating electrode materials in practical application. For the CS/Se/HCS-0.3/S electrode, a reversible capacity of 480 mA h g^{-1} can still be maintained at a high rate of 3 C after 200 cycles (Fig. 3b). Figure 3c exhibits the long cycling performances of the three electrodes at 1 C. The initial specific discharge capacities of the CS/Se/HCS-0.2/S, CS/Se/HCS-0.3/S, and CS/Se/HCS-0.4/S electrodes are 705, 1089, and 694 mA h g^{-1}, with initial coulombic efficiencies of 87%, 92%, and 86%, respectively. The capacities of the three electrodes remain 210, 413, and 266 mA h g^{-1} after 500 cycles, respectively. Rate performances of the prepared samples are tested at 0.1–3 C rate, at 0.1, 0.2, 0.5, 1, 2, and 3 C, and the specific capacities of CS/Se/HCS-0.3/S electrode are 1184, 985, 847, 763,

679 and 628 mA h g^{-1}, respectively (Fig. 3d). When the C rate returns to 0.1 C, the specific capacity can be recovered to 920 mA h g^{-1}, suggesting that the electrode has good tolerance to current changes. It is obvious that the specific capacities of the CS/Se/HCS-0.2/S and CS/Se/HCS-0.4/S electrodes are significantly lower than those of the CS/Se/HCS-0.3/S electrode at each rate. The cycling performance of the HCS/S electrode was also studied, and the result is shown in Figure S4. After 300 cycles, the specific capacity of the HCS/S electrode is 227 mA h g^{-1}, which is much lower than that of the CS/Se/HCS/S electrodes. The CS/Se/HCS-0.3/S electrode also exhibits satisfactory electrochemical performance with a higher sulfur loading of 5.0 mg cm^{-2}, which can present an initial discharge specific capacity of 695 mA h g^{-1}, and the capacity can be maintained at 446 mA h g^{-1} after 50 cycles (Figure S5). The electrochemical performance tests proved that the CS/Se/HCS-0.3/S electrode had the best electrochemical performance, which is attributed to the special 3D structure and the suitable $CoSe_2$/Se content. Additionally, in Table S1, we make a comparison of related sulfur hosts in the literature with this work. Compared with other similar sulfur hosts, the CS/Se/HCS-0.3/S electrode exhibits superior electrochemical performance, especially at high rates [50–57].

The electrochemical reaction mechanism of the CS/Se/HCS-0.3 host with excellent performance was investigated by CV, UV, and EIS. Typical CV profiles of the CS/Se/HCS-0.2/0.3/0.4/S electrodes tested at 0.1 mV s^{-1} are given in Fig. 4a. Two cathodic peaks at 2.30 and 2.04 V appearing in the CS/Se/HCS-0.3/S electrode are assigned to the reduction of S_8 to long-chain LPSs and the long-chain LPSs to Li_2S, respectively. The two anodic peaks correspond to the transformation of Li_2S into LPSs and S_8 again; meanwhile, the obvious split anodic peaks indicate that the CS/Se/HCS-0.3/S electrode has good electrocatalytic performance and can accelerate the oxidation process of sulfur cathode [58–60]. Furthermore, the voltage difference (ΔE) between the anodic peak and cathodic peak can reflect the dynamic performance of an electrode; it is worth noting that the ΔE of CS/Se/HCS-0.3/S electrode is the smallest, indicating that it has better dynamic performance than other electrodes [61]. Furthermore, except the first cycle, the CV profiles of the CS/Se/HCS-0.3/S electrode show good coincidence in the following cycles (Figure S6), suggesting the excellent reversibility of the CS/Se/HCS-0.3/S electrode [11, 24]. Figure 4b illustrates the initial charge–discharge curves of the CS/Se/HCS-0.2/0.3/0.4/S electrodes at 0.5 C; and the voltage difference between charge and discharge plateaus of the CS/Se/HCS-0.3/S electrode is 0.05 V, which is significantly smaller than that of the CS/Se/HCS-0.2/S (0.18 V) and CS/Se/HCS-0.4/S electrodes (0.21 V), and the result is consistent with the CV [21, 26]. Meanwhile, the charge–discharge platform of the CS/Se/HCS-0.3/S electrode is longer, illustrating that the electrode has a higher specific capacity. In addition, the voltage drop of the CS/Se/HCS-0.3/S electrode in the initial charging process is significantly lower than that of other electrodes, indicating the improved kinetics of Li_2S nucleation in this electrode [12, 28]. To explore the adsorption performance of the CS/Se/HCS-0.3 host toward LPSs, UV adsorption test was performed. Immerse CS/Se/HCS-0.3 in the prepared Li_2S_6 solution, the orange solution becomes clear after 4 h (Fig. 4c), illustrating the lower S_6^{2-} concentration in the solution. Furthermore, the UV adsorption curve showed that the S^{2-} characteristic peak at 423 nm disappears, illustrating that the CS/Se/HCS-0.3 host has excellent adsorption performance toward LPSs [62, 63]. To study the electrochemical catalytic performance of the CS/Se/HCS hosts, CV tests of symmetrical batteries in a potential range of − 0.8–0.8 V were performed. The results are shown in Figure S11; it can be seen that the CS/Se/HCS-0.3 host exhibits a higher peak current, indicating the better electrochemical catalytic of CS/Se/HCS-0.3.

Figure 4d exhibits the EIS plots of the CS/Se/HCS-0.2/0.3/0.4/S electrodes. The semicircle in the high-frequency region corresponds to the electron transfer resistance of an electrode, and the straight line in the low-frequency region is related to lithium-ion diffusion. The CS/Se/HCS-0.3/S electrode presents a smaller radius of curvature, indicating that the electrode has a lower electron transfer resistance. This is because the electrode contains more Se, which makes the electrode have better high rate performance [17, 57]. The corresponding Weber impedance diagrams are shown in Figure S7; based on the EIS results, the Li^+ diffusion coefficient of the CS/Se/HCS-0.2/S, CS/Se/HCS-0.3/S, and CS/Se/HCS-0.4/S electrodes are 1.8×10^{-12}, 7.9×10^{-12}, and 4.4×10^{-12} cm^2 s^{-1}, respectively. In addition, CS/Se/HCS-0.3 electrode still exhibits smaller charge

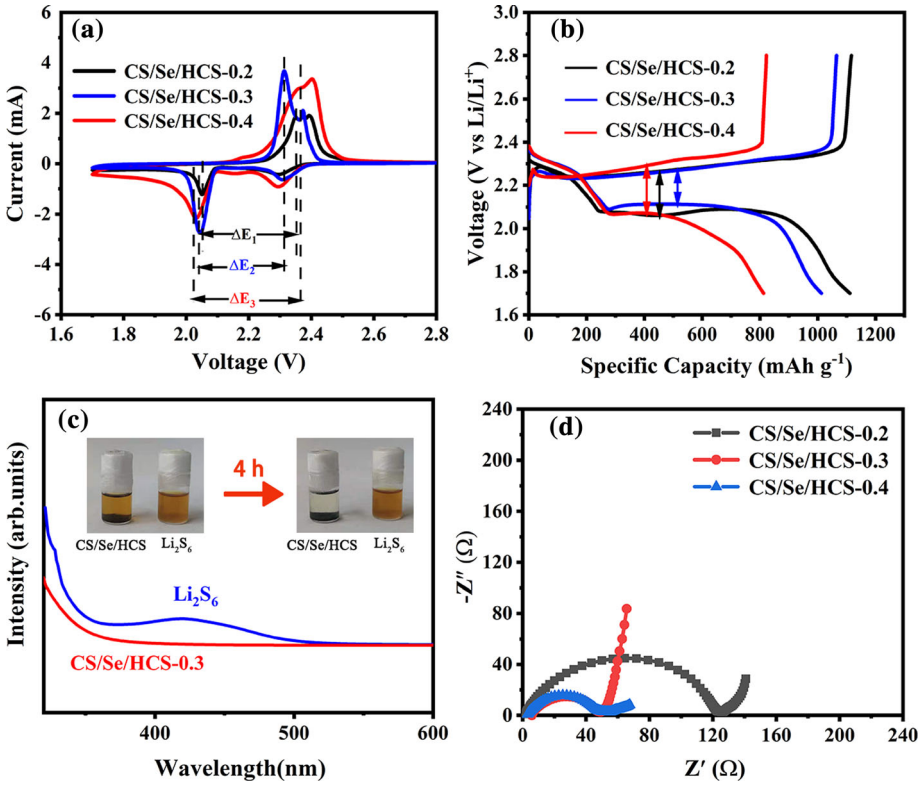

Figure 4 **a** CV curves of CS/Se/HCS-0.2/0.3/0.4/S electrodes at 0.1 mV s^{-1} and **b** charging–discharging curves of the CS/Se/HCS-0.2/0.3/0.4/S electrodes at 0.5 C. **c** Adsorption test and UV spectra of the CS/Se/HCS-0.3 in Li_2S_6 solution. **d** EIS plots of the CS/Se/HCS-0.2/0.3/0.4/S electrodes.

transfer resistance after 100 cycles (Figure S8), illustrating the superior structural stability of the electrode.

The charge storage behavior and capacitive contribution were investigated by CV. CV curves at various scan rates of the CS/Se/HCS-0.3/S electrode and the corresponding b value are demonstrated in Fig. 5a and b. As it is reported that the b values of 0.5 and 1.0 correspond to diffusion and surface control behavior of an electrode during the electrochemical process, respectively [64]. For the CS/Se/HCS-0.3/S electrode, the b values of the four redox peaks are 0.54, 0.71, 0.37, and 0.72, respectively, suggesting that the charge storage in this electrode is mainly controlled by diffusion behavior. The capacities of LSBs are mainly contributed by the conversion between LiPSs and Li_2S; therefore, an electrode with a high Li^+ diffusion rate delivers an excellent rate performance [65, 66]. In the EIS tests, we have gotten the results that the Li^+ diffusion rate in CS/Se/HCS-0.3 electrode is the fastest; therefore, the CS/Se/HCS-0.3 electrode presents the best electrochemical performance. As shown in Fig. 5c, the pseudo-capacitance contribution ratio of the CS/Se/HCS-0.3 composite is 34.12% at 0.2 mV s^{-1}. At scan rates of 0.2, 0.4, 0.6, 0.8, and 1.0 mV s^{-1}, Fig. 5d shows that 66%, 60%, 57%, 56%, and 52% of the total capacities are contributed by diffused contribution.

SEM image characterization of Li metal anode after 100 cycles was utilized to study the anode surface. After cycling, the lithium deposition is relatively uniform, and there is no obvious dendrite formation on the surface of Li metal anode (Figure S9). This result also proves that the CS/Se/HCS-0.3 host can limit the shuttle of LPSs. Meanwhile, in Figure S10 the morphology of the CS/Se/HCS-0.3/S cathode after cycles was studied by SEM; it is found that the structure of the cathode before and after cycling does not change significantly and the nanorods can be obviously detected, suggesting the superior stability of the electrode.

Conclusion

In summary, we successfully designed and prepared 3D-structured CS/Se/HCS sulfur hosts for LSBs using hollow carbon spheres as templates. The 3D structure of the host is conducive to the transport of Li^+ and electrons, and the hollow carbon sphere is beneficial to suppress the volume change of the S electrode during charge and discharge processes;

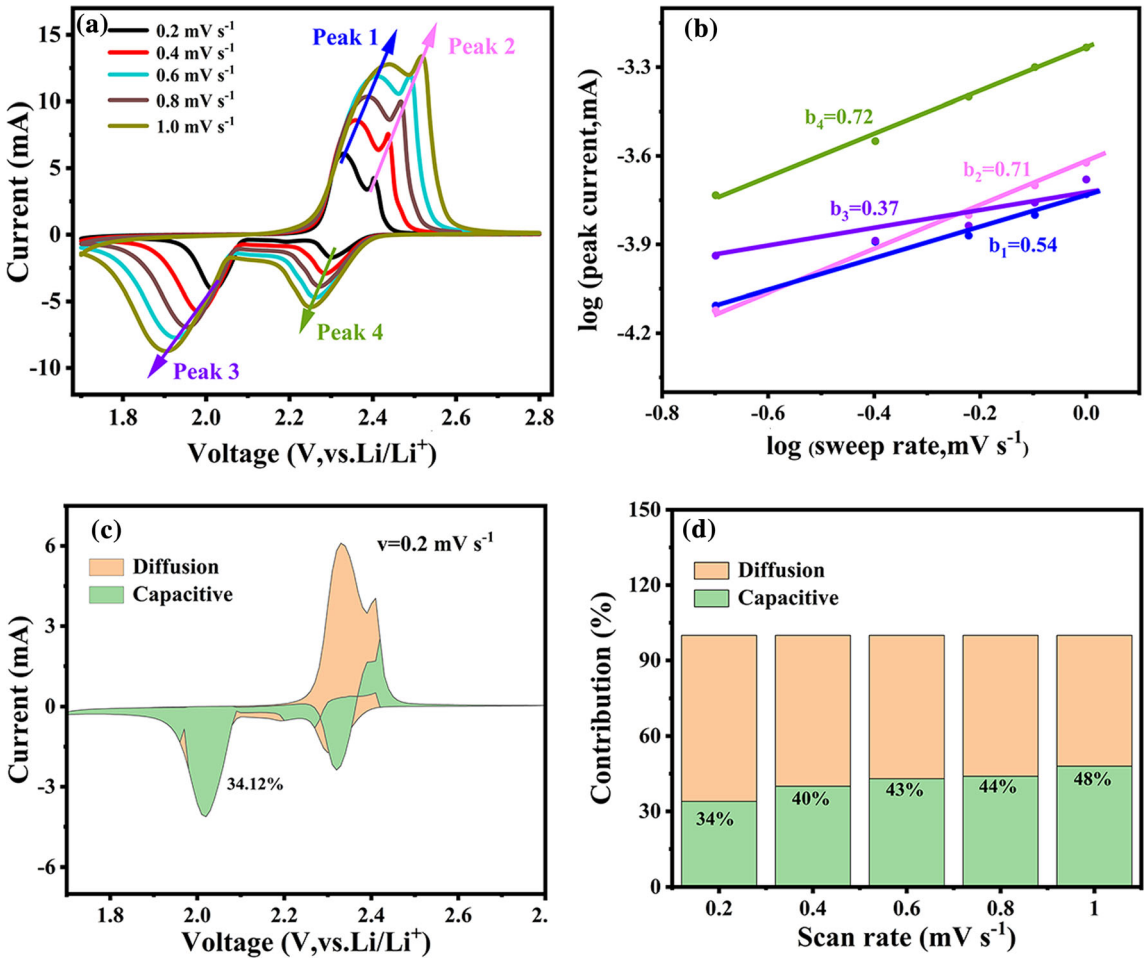

Figure 5 CV curves of the CS/Se/HCS-0.3/S electrode at different scan rates (**a**); corresponding b value of the CS/Se/HCS-0.3/S electrode (**b**); capacitive contribution and diffusion-controlled contribution of the CS/Se/HCS-0.3/S electrode at 0.2 mV s^{-1}; (**d**) diagram of capacitive contribution to the total capacity of the CS/Se/HCS-0.3/S electrode at different scan rates.

meanwhile, the shuttle of LPSs is alleviated to a certain extent through physical confinement. The $CoSe_2$/Se can inhibit LPSs shuttle through chemical adsorption and accelerate their conversion. Electrochemical tests demonstrate that the CS/Se/HCS-0.3/S electrode exhibits the best performance; at 1 C, it can achieve a specific capacity of 424 mA h g^{-1} after 500 cycles. At high rates of 2 and 3C, the specific capacities of the electrode can reach 597 and 591 mA h g^{-1} after 200 cycles, respectively. Furthermore, the specific capacity of the electrode with the sulfur loading of 5.0 mg cm^{-2} can be maintained at 446 mA h g^{-1} after 50 cycles. This work provided a new idea for the application of hollow carbon spheres and transition metal selenide in LSBs.

Acknowledgements

This work was financially supported by Natural Science Foundation of Shandong Province (Grant No. ZR2022ME062 and ZR2021QE175), Jinan Talent Project (2020GXRC044), the New Colleges and Universities Twenty Foundational Projects of Jinan City (2021GXRC068), Qilu University of Technology International Cooperation Fund (QLUTGJHZ2018025), and Innovative Talent Exchange Foreign Expert Talent Program (DL2021023005L).

Data and code availability

Not Applicable.

Declarations

Conflict of interest I'm the corresponding author of this manuscript. I on behalf all the authors state that this publication is approved by all authors and there is no conflict of interest between the authors.

Ethical approval Not Applicable.

Supplementary Information: The online version contains supplementary material available at https://doi.org/10.1007/s10853-023-08631-z.

References

[1] Li N, Chen F, Chen X et al (2020) A bipolar modified separator using TiO_2 nanosheets anchored on N-doped carbon scaffold for high-performance Li–S batteries. J Mater Sci Technol 55:152–158

[2] Liu A, Liang X, Ren X et al (2022) Recent progress in MXene-based materials for metal–sulfur and metal-air batteries: potential high-performance electrodes. Electrochem Energy Rev 5:112–114

[3] Chang F, Xiao M, Miao R et al (2022) Copper-based catalysts for electrochemical carbon dioxide reduction to multicarbon products. Electrochem Energy Rev 5:4

[4] Ding XW, Yang S, Zhou SY et al (2020) Biomimetic molecule catalysts to promote the conversion of polysulfides for advanced lithium–sulfur batteries. Adv Funct Mater 30:2003354

[5] Xu W, Wu Q, Che Z et al (2021) A novel synthesizing strategy of 3D $CoSe_2$ porous hollow flowers for high performance lithium–sulfur batteries. Catalysts 11:273

[6] Su H, Lu L, Yang M et al (2022) Decorating $CoSe_2$ on N-doped carbon nanotubes as catalysts and efficient polysulfides traps for Li–S batteries. Chem Eng J 429:132167

[7] Kim J, Shin H, Yoo DJ et al (2021) Cobalt(II)-centered fluorinated phthalocyanine-sulfur SNAr chemistry for robust lithium–sulfur batteries with superior conversion kinetics. Adv Funct Mater 31:2106679

[8] Wang JJ, Cao GQ, Duan RX et al (2023) Advances in single metal atom catalysts enhancing kinetics of sulfur cathode. Acta Phys -Chim Sin 39:2212005

[9] Li Z, Wu HB, Lou XW (2016) Rational designs and engineering of hollow micro-/nanostructures as sulfur hosts for advanced lithium–sulfur batteries. Energy Environ Sci 9:3061

[10] Zhang J, Huang H, Bae J et al (2018) Nanostructured host materials for trapping sulfur in rechargeable Li–S batteries: structure design and interfacial chemistry. Small Methods 2:1700279

[11] Dai CL, Lim JM, Wang MQ et al (2018) Honeycomb-like spherical cathode host constructed from hollow metallic and polar Co_9S_8 tubules for advanced lithium–sulfur batteries. Adv Funct Mater 28:1704443

[12] Zhang C, Biendicho JJ, Zhang T et al (2019) Combined high catalytic activity and efficient polar tubular nanostructure in urchin-like metallic $NiCo_2Se_4$ for high-performance lithium–sulfur batteries. Adv Funct Mater 29:1903842

[13] Agostini M, Lim DH, Sadd M et al (2018) Rational design of low cost and high energy lithium batteries through tailored fluorine-free electrolyte and nanostructured S/C composite. Chemsuschem 11:2981–2986

[14] Lin ZQ, Zeng ZP, Gui XC et al (2016) Carbon nanotube sponges, aerogels, and hierarchical composites: synthesis, properties, and energy applications. Adv Energy Mater 6:26–30

[15] Pei F, An TH, Zang J et al (2016) From hollow carbon spheres to N-doped hollow porous carbon bowls: rational design of hollow carbon host for Li–S batteries. Adv Energy Mater 6:1502539

[16] Zhang CF, Wu HB, Yuan CZ et al (2012) Confining sulfur in double-shelled hollow carbon spheres for lithium–sulfur batteries. Angew Chem Int Ed 51:9592–9595

[17] Chen B, Zhong XW, Zhou GM et al (2022) Graphene-supported atomically dispersed metals as bifunctional catalysts for next-generation batteries based on conversion reactions. Adv Mater 34:2105812

[18] Xia L, Wang SQ, Liu GX et al (2016) Flexible SnO_2/N-doped carbon nanofiber films as integrated electrodes for lithium–ion batteries with superior rate capacity and long cycle life. Small 12:853–859

[19] Peng HJ, Zhang G, Chen X et al (2016) Enhanced electrochemical kinetics on conductive polar mediators for lithium–sulfur batteries. Angew Chem Int Ed 55:12990–12995

[20] He YY, Wang L, Dong CF et al (2019) In-situ rooting ZnSe/N-doped hollow carbon architectures as high-rate and long-life anode materials for half/full sodium-ion and potassium-ion batteries. Energy Stor Mater 23:35–45

[21] Yang D, Zhang C, Biendicho JJ et al (2020) ZnSe/N-doped carbon nanoreactor with multiple adsorption sites for stable lithium–sulfur batteries. ACS Nano 14:15492–15504

[22] He J, Luo L, Chen Y, Manthiram A (2017) Yolk-shelled C@Fe_3O_4 nanoboxes as efficient sulfur hosts for high-performance lithium–sulfur batteries. Adv Mater 29:1702707

[23] Han Z, Gao R, Jia Y et al (2022) Catalytic effect in Li–S batteries: from band theory to practical application. Mater Today 57:84–120

[24] Chen T, Ma LB, Cheng BR et al (2017) Metallic and polar Co_9S_8 inlaid carbon hollow nanopolyhedra as efficient polysulfide mediator for lithium-sulfur batteries. Nano Energy 38:239–248

[25] Xiao ZB, Yang Z, Zhang LJ et al (2017) Sandwich-type NbS_2@S@I-doped graphene for high-sulfur-loaded, ultra-high-rate, and long-life lithium sulfur batteries. ACS Nano 11:8488–8498

[26] Kong L, Li BQ, Peng HJ et al (2018) Porphyrin-derived graphene-based nanosheets enabling strong polysulfide chemisorption and rapid kinetics in lithium–sulfur batteries. Adv Energy Mater 8:1800849

[27] Cao GQ, Duan RX, Li XF (2022) Controllable catalysis behavior for high performance lithium sulfur batteries: from kinetics to strategies. EnergyChem 5:100096

[28] Deng DR, Xue F, Jia YJ et al (2017) Co_4N nanosheet assembled mesoporous sphere as a matrix for ultrahigh sulfur content lithium–sulfur batteries. ACS Nano 11:6031–6039

[29] Lin H, Yang L, Jiang X et al (2017) Electrocatalysis of polysulfide conversion by sulfur-deficient MoS_2 nanoflakes for lithium–sulfur batteries. Energy Environ Sci 10:1476–1486

[30] Liu DH, Zhang C, Zhou GM et al (2018) Catalytic effects in lithium-sulfur batteries: promoted sulfur transformation and reduced shuttle effect. Adv Sci 5:1700270

[31] Tian Y, Li GR, Zhang YG et al (2020) Low-bandgap Se-deficient antimony selenide as a multifunctional polysulfide barrier toward high-performance lithium–sulfur batteries. Adv Mater 32:1904876

[32] Yuan H, Peng HJ, Li BQ et al (2019) Conductive and catalytic triple-phase interfaces enabling uniform nucleation in high-rate lithium–sulfur batteries. Adv Energy Mater 9:1802768

[33] Chen L, Xu Y, Cao G et al (2021) Bifunctional catalytic effect of $CoSe_2$ for lithium–sulfur batteries: single doping versus dual doping. Adv Func Mater 32:2107838

[34] Li Y, Wang XZ, Sun MH, et al (2022) CoSe nanoparticle embedded B,N-codoped carbon nanotube array as a dual-functional host for a high-performance Li–S full battery. Acs Nano 16:17008–17020

[35] Boyjoo Y, Shi HD, Olsson E et al (2020) Molecular-level design of pyrrhotite electrocatalyst decorated hierarchical porous carbon spheres as nanoreactors for lithium–sulfur batteries. Adv Energy Mater 10:200651

[36] Perez-Lorenzo M, Vaz B, Salgueirino V et al (2013) Hollow-shelled nanoreactors endowed with high catalytic activity. Chem Eur J 19:12196–12211

[37] Ye Z, Jiang Y, Yang T et al (2022) Engineering catalytic CoSe–ZnSe heterojunctions anchored on graphene aerogels for bidirectional sulfur conversion reactions. Adv Sci 9:2103456

[38] Zhong W, Lv X, Chen Q et al (2019) Metal-organic framework/polythiophene derivative: neuronlike S-doped carbon 3D structure with outstanding sodium storage performance. ACS Appl Mater Interfaces 11:37850–37858

[39] Yousaf M, Chen YJ, Tabassum H et al (2020) A dual protection system for heterostructured 3D CNT/$CoSe_2$/C as high areal capacity anode for sodium storage. Adv Sci 7:1902907

[40] Ge P, Hou H, Li S et al (2018) Three-dimensional hierarchical framework assembled by cobblestone-like $CoSe_2$@C nanospheres for ultrastable sodium–ion storage. ACS Appl Mater Interfaces 10:14716–14726

[41] Kong DS, Wang HT, Lu ZY et al (2014) $CoSe_2$ nanoparticles grown on carbon fiber paper: an efficient and stable electrocatalyst for hydrogen evolution reaction. J Am Chem Soc 136:4897–4900

[42] Chen Q, Zhong W, Zhang J et al (2019) Fe_3O_4 nanorods in N-doped carbon matrix with pseudo-capacitive behaviors as an excellent anode for subzero lithium–ion batteries. J Alloys Compd 772:557–564

[43] Jin KK, Park GD, Kim JH et al (2017) Rational design and synthesis of extremely efficient macroporous $CoSe_2$-CNT composite microspheres for hydrogen evolution reaction. Small 13:1700068

[44] Zhao B, Liu Q, Wei G et al (2019) Synthesis of $CoSe_2$ nanoparticles embedded in N-doped carbon with conformal TiO_2 shell for sodium–ion batteries. Chem Eng J 378:122206

[45] Guo H, Liu G, Wang M et al (2020) In-situ fabrication of bone-like $CoSe_2$ nano-thorn loaded on porous carbon cloth as a flexible electrode for Na–ion storage. Chem Asian J 15:1493–1499

[46] Zhang K, Park M, Zhou L et al (2016) Urchin-like $CoSe_2$ as a high-performance anode material for sodium–ion batteries. Adv Funct Mater 26:6728–6735

[47] Sakthivel M, Ramaraj S, Chen S-M et al (2019) Bimetallic vanadium cobalt diselenide nanosheets with additional active sites for excellent asymmetric pseudocapacitive performance: comparing the electrochemical performances with M-$CoSe_2$ (M = Zn, Mn, and Cu). J Mater Chem A 7:12565–12581

[48] Liu X, Xu GB, Cheng TT et al (2020) Effect of crystal structures on electrochemical performance of hierarchically porous $CoSe_2$ spheres as anodes for sodium–ion batteries. ChemElectroChem 7:846–854

[49] Zhang J, Fan L, Zhu Y et al (2014) Selenium/interconnected porous hollow carbon bubbles composites as the cathodes of Li–Se batteries with high performance. Nanoscale 6:12952–12957

[50] Yu XF, Li WC, Hu YR et al (2021) Sculpturing solid polymer spheres into internal gridded hollow carbon spheres under controlled pyrolysis micro-environment. Nano Res 14:1565–1573

[51] Xu F, Tang Z, Huang S et al (2015) Facile synthesis of ultrahigh-surface-area hollow carbon nanospheres for enhanced adsorption and energy storage. Nat Commun 6:7221

[52] Li X, Cheng X, Gao M et al (2017) Amylose-derived macrohollow core and microporous shell carbon spheres as sulfur host for superior lithium–sulfur battery cathodes. ACS Appl Mater Interfaces 9:10717–10729

[53] Zhou G, Zhao Y, Manthiram A (2015) Dual-confined flexible sulfur cathodes encapsulated in nitrogen-doped double-shelled hollow carbon spheres and wrapped with graphene for Li–S batteries. Adv Energy Mater 5:1402263

[54] Wu F, Li J, Su Y et al (2016) Layer-by-layer assembled architecture of polyelectrolyte multilayers and graphene sheets on hollow carbon spheres/sulfur composite for high-performance lithium–sulfur batteries. Nano Lett 16:5488–5494

[55] Wu Z, Wang W, Wang Y et al (2017) Three-dimensional graphene hollow spheres with high sulfur loading for high-performance lithium-sulfur batteries. Electrochim Acta 224:527–533

[56] Zhang Y, Zong X, Zhan L et al (2018) Double-shelled hollow carbon sphere with microporous outer shell towards high performance lithium–sulfur battery. Electrochim Acta 284:89–97

[57] Cheng J, Liu Y, Zhang X et al (2021) Structure engineering in interconnected porous hollow carbon spheres with superior rate capability for supercapacitors and lithium–sulfur batteries. Chem Eng J 419:129649

[58] Li YJ, Wu JB, Zhang B et al (2020) Fast conversion and controlled deposition of lithium (poly)sulfides in lithium-sulfur batteries using high-loading cobalt single atoms. Energy Stor Mater 30:250–259

[59] Zhou GM, Tian HZ, Jin Y et al (2017) Catalytic oxidation of Li_2S on the surface of metal sulfides for Li–S batteries. Proc Natl Acad Sci U S A 114:840–845

[60] Shen Z, Zhang Z, Li M et al (2020) Rational design of a $Ni_3N_{0.85}$ electrocatalyst to accelerate polysulfide conversion in lithium–sulfur batteries. ACS Nano 14:6673–6682

[61] Li ZH, He Q, Xu X et al (2018) A 3D nitrogen-doped graphene/TiN nanowires composite as a strong polysulfide anchor for lithium–sulfur batteries with enhanced rate performance and high areal capacity. Adv Mater 30:1804089

[62] Song J, Yu Z, Gordin ML et al (2016) Advanced sulfur cathode enabled by highly crumpled nitrogen-doped graphene sheets for high-energy-density lithium–sulfur batteries. Nano Lett 16:864–870

[63] Li X, Ding K, Gao B et al (2017) Freestanding carbon encapsulated mesoporous vanadium nitride nanowires enable highly stable sulfur cathodes for lithium–sulfur batteries. Nano Energy 40:655–662

[64] Wang J, Wang J, Han L et al (2019) Fabrication of an anode composed of a N, S co-doped carbon nanotube hollow architecture with CoS_2 confined within: toward Li and Na storage†. Nanoscale 11:20996–21007

[65] Chen X, Xu Y, Du FH, Wang Y (2019) Covalent organic framework derived boron/oxygen codoped porous carbon on CNTs as an efficient sulfur host for lithium–sulfur batteries. Small Methods 3:1900338

[66] Huang S, Lim YV, Zhang X et al (2018) Regulating the polysulfide redox conversion by iron phosphide nanocrystals for high-rate and ultrastable lithium–sulfur battery. Nano Energy 51:340–348